Accurate Real-Time Laser Spot Locating Based on Template Correlation in Intersatellite Laser Communications

Xiangsheng Meng, Wen Liu, Junfeng Han, Yan Tian, Jun Liu, and Caiwen Ma

***Abstract*—In intersatellite laser communications, the centroiding accuracy of a laser spot is crucial for maintaining steady communication links. However, the systematic error introduced by discrete sampling restricts further improvement of centroiding accuracy when choosing algorithms that are widely used in engineering. Additionally, the ultrahigh computational complexity and multiple-step iterations of the Gaussian fitting (GF) algorithm are unsuitable for real-time implementation, even though the algorithm can achieve the highest centroiding accuracy. In this study, we propose a laser spot centroiding algorithm based on template correlation to simultaneously satisfy the requirements of real-time performance and accuracy. The proposed algorithm evaluates the central location of a laser spot by obtaining the index of the maximum Pearson correlation coefficient (PCC). Simulations performed under different conditions reveal that the proposed algorithm is robust against the interference of background noise and the bad pixels. Moreover, experimental verification is performed based on the implementation on a Field-Programmable Gate Array (FPGA) in real-time, meanwhile its accuracy is on the same level as that of the GF algorithm and better than those of other widely-used algorithms. Therefore, the proposed algorithm is suitable for accurate real-time locating of laser spots in engineering applications of the intersatellite laser communications.**

***Index Terms*—Intersatellite laser communications, centroiding accuracy, real-time, engineering applications.**

I. Introduction

CURRENTLY, with the increasing space explorations, various satellites in orbit always generate huge amounts of scientific data; thus, the demand for the transmission bandwidth of satellites has risen [1]. Traditional microwave communications, restricted by their technical bottlenecks, cannot satisfy the demands of rapidly transmitting mass data between satellites [2]. However, owing to the advantages of large bandwidth, free-space laser communications can establish high-speed, low-intercept intersatellite communications, which is considered a solution for this limitation [3], [4]. Encouraged by the in-orbit operation of OneWeb and Starlink constellations, several large low-Earth-orbit constellations are expected to establish a global broadband satellite network, among which the laser communication terminals (LCTs) act as key payloads to realize intersatellite high-speed data transactions [5], [6], [7], [8]. In October 2013, NASA's bidirectional moon-to-earth laser communication program, lunar laser communication demonstration (LLCD), achieved downlink and uplink data rates of 622 Mbps and 20 Mbps, respectively, which established the foundation for deep space exploration using LCTs [9], [10], [11].

In intersatellite laser communications(ILC), communication links are maintained by tracking the laser spot, which is the diffraction image of parallel light in the image plane, and the intensity conforms to the Airy disk [12]. During the tracking procedure, a photoelectric sensor samples and quantizes the laser spot into gray images, which are output to the processor to precisely calculate the error between the actual and expected locations. Subsequently, the error, which represents boresight misalignment, is introduced into the closed loop by the tracking controller such that the lines of sight can align. Therefore, the accuracy of the actual location calculation is significant for the reliability of intersatellite laser communications.

Many classical algorithms have been proposed for laser spot centroids. Theoretically, the Gaussian fitting (GF) algorithm can achieve the highest accuracy [13] because the Airy disk can be approximated using a two-dimensional Gaussian function [14]. As for the engineering application, the center of gravity (CG), center of gravity with threshold (CGT), and filtered center of gravity (FCG) algorithms are most commonly used. However, because the GF algorithm is a nonlinear fitting method, multiple-step iterations and inverse matrix computation inevitably produce problems such as instability and time consumption during implementation. The CG algorithm has a weak noise robustness [15] and contains systematic error that introduced by discrete sampling [16]. The CGT algorithm can strengthen noise robustness to a certain extent [17], [18], but the truncation error [19] limits its accuracy. The FCG algorithm changes the gray-scale distribution of the spot and inevitably introduces a centroiding error.

Algorithms about improving the performance have been proposed regard to laser communication field. Ref [20] improves

Manuscript received 27 August 2023; revised 6 November 2023; accepted 17 November 2023. Date of publication 28 November 2023; date of current version 26 December 2023. This work was supported by the National Key Research and Development Program of China under Grants 2022YFC2203800 and 2022YFC30026. *(Corresponding authors: Xiangsheng Meng; Wen Liu.)*

The authors are with the Key Laboratory of Space Precision Measurement Technology, Xi'an Institute of Optics and Precision Mechanics, Chinese Academy of Sciences, Xi'an 710119, China, and also with the University of Chinese Academy of Sciences, Beijing 100049, China (e-mail: mengxiangsheng@opt.ac.cn; wliu@opt.ac.cn; hanjf@opt.ac.cn; ty_cas@163.com; liujun1@opt.ac.cn; cwma@opt.ac.cn).

Digital Object Identifier 10.1109/JPHOT.2023.3335234

the CG accuracy by regional interpolation. As the centroiding method is still the CG, the proposed method will inevitablely sensitive to the noise. Ref [21] predicts the centroid based on machine learning to overcome the nonlinear disturbances. However, it's not suitable for in-orbit application as the complexity. Ref [22] combines the edge detection and Kalman filter (KF) to achieve a good robustness to turbulence, but the accuracy is relatively low compared to the classical algorithms when using in the ILC. Ref [23] combines the squared weighting centroid algorithm and the interpolation subdivision algorithm to improve the locating accuracy, but the noise robustness is still weak.

In this study, we focus on simultaneously improving the accuracy, the noise robustness and the real-time performance of the laser spot centroiding algorithm. We propose a laser spot centroiding algorithm based on template correlation. The basic principles of the proposed algorithm are described in Section II. The simulations of different situations are presented in Section III, and in Section IV, the algorithm is implemented on a Field-Programmable Gate Array (FPGA) and verified in the LCT indoor experimental system. Finally, the conclusions of the study are presented in Section V.

II. Basic Principles

A. Basic Principles of Laser Spot

As mentioned earlier, the laser spot of a focal plane can be approximated by a Gaussian function, which is expressed as [18]:

$$I(x,y\,|x_0,y_0\,) = I_0 \exp\left(-\frac{(x-x_0)^2+(y-y_0)^2}{2\sigma^2}\right) \quad (1)$$

where I_0 indicates the peak of the spot; x_0 and y_0 denote the centroid of the spot; and σ represents the radius of the laser spot.

According to the diffraction imaging theory, the diameter of a laser spot in a focal plane is defined as [12]:

$$dia = \frac{2.44 \times \lambda \times f}{D} \quad (2)$$

where λ, f, and D represent the wavelength, focal length, and aperture of the telescope, respectively. All three parameters are invariant because the system design has been confirmed; thus, σ can naturally be assumed as constant when approximating the laser spot to a Gaussian function.

Laser spot imaging involves discrete sampling and digital quantization. The laser spot intensity function $I(x, y|\ x_0, y_0)$ convolve the pixel sensitivity profile $P(x, y)$ to obtain the pixel energy-receiving function $f(x, y)$, as follows [14].

$$f(x,y) = I(x,y\,|x_0,y_0\,) \otimes P(x,y) \quad (3)$$

The pixel sensitivity profile with pixel width d can be obtained as follows [24].

$$P(x,y) = \begin{cases} \frac{1}{d^2}, & -d/2 < x,y < d/2 \\ 0, & x,y < -d/2 \&\& x,y > d/2 \end{cases} \quad (4)$$

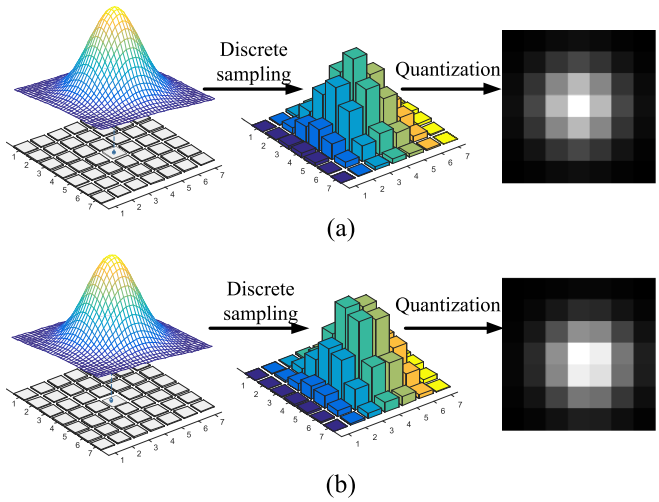

Fig. 1. Schematic of the laser-spot imaging process. (a) Coincident center. (b) Displaced center.

Next, $f(x, y)$ multiply the sampling function $s(x, y)$ to yield the sampled function $g(x, y)$ [24]:

$$g(x,y) = f(x,y) \times s(x,y) \quad (5)$$

The sampling function $s(x, y)$ is a comb function [14], where d denotes the pixel width.

$$s(x,y) = comb(x/d, y/d) \quad (6)$$

Finally, the discrete sampled function $g(x, y)$ is quantized to a grayscale image.

Fig. 1(a) shows the imaging process for an ideal situation in which the laser spot centroid and pixel center coincide. Here, x_0 and y_0 are integers, the spot image is symmetrical, and almost all the algorithms can achieve high centroiding accuracy. However, the actual situation in the system application is that the laser spot centroid and pixel center are displaced; thus, the grayscale image is dissymmetrical, as shown in Fig. 1(b).

The whole imaging process can be formularized by (7), which is derived by substituting (3), (4), and (6) into (5).

$$g(x,y) = [I(x,y\,|x_0+\Delta x, y_0+\Delta y\,) \otimes P(x,y)] \times s(x,y) \quad (7)$$

As mentioned earlier, finite-width discrete sampling introduces a system error and affects the subpixel displacement estimation when the grey-level information is used as weights to calculate the centroid.

B. Basic Principles of the Proposed Algorithm

The displaced imaging process defined by (7) can be derived as (8), which indicates that the laser spot is immobile but the sampling function is displaced.

$$g(x,y) = [I(x,y\,|x_0,y_0\,) \otimes P(x,y)] \times s(x,y\,|\Delta x, \Delta y\,) \quad (8)$$

In this situation, the sampling function with displacement is represented as:

$$s(x,y\,|\Delta x, \Delta y\,) = comb(x+\Delta x/d, y+\Delta y/d) \quad (9)$$

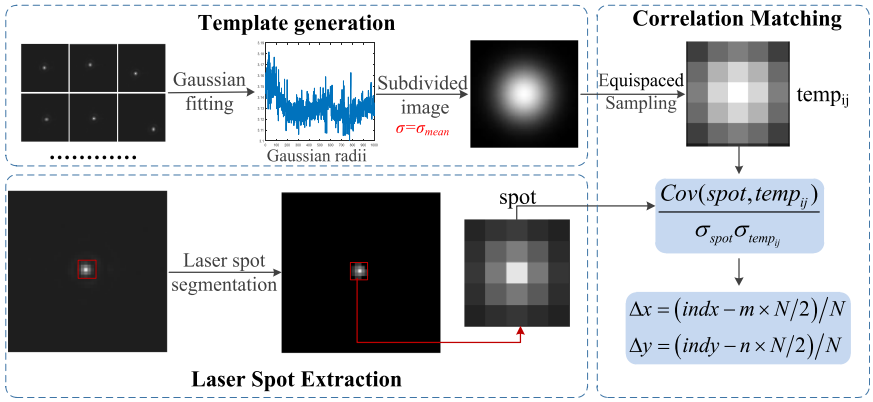

Fig. 2. Framework of the proposed method.

We can obtain a series of laser spot images with different centroids by changing Δx and Δy in (9), and in theory we can find a similar one with the displaced spot image from the image sequences as long as Δx and Δy are small enough.

Therefore, the key objective of the proposed algorithm is to determine the displacement of the sampling function, which is obtained by maximum correlation matching. The framework of the proposed method is illustrated in Fig. 2.

The procedure of the method is described as follows. First, several laser spot images are captured by pointing the LCT to the collimator, followed by fitting the captured laser spots to the Gaussian function. Subsequently, the Gaussian radii of the laser spots are calculated and represented by σ, and all radii are averaged to obtain σ_{mean}. Subsequently, an N-fold subdivided template image is generated by setting the parameters $I_0 = 255$, $x_0 = 0$, $y_0 = 0$, and $\sigma = \sigma_{mean}$.

The spot image is extracted from the camera's grayscale image and denoted as *spot* with a size of $m \times n$. Comparable images are constructed by sampling the template image every N pixels, which are indicated as $temp_{ij}$. The comparable images are a series of images that are equispaced sampled from the N-fold subdivided template image. as shown in Fig. 3 which is an example when $N = 5$, $m = n = 3$.

The method is further explained as follows. The size of the N-fold subdivided template image is $N{\times}m \times N{\times}n$. We can obtain the $m \times n$ comparable image by equidistant sampling the template image when the sample interval is N pixel. By changing the start positon we can get a series of images in which there must be one image that almost the same with the spot image. The similarity between spot image and comparable image is determined by Pearson correlation coefficient (PCC) which is calculated as [25]:

$$\rho_{ij} = \frac{Cov(spot, temp_{ij})}{\sigma_{spot}\sigma_{temp_{ij}}} = \frac{\sum_m \sum_n \left(spot_{mn} - \overline{spot}\right)\left([temp_{ij}]_{mn} - \overline{temp_{ij}}\right)}{\sqrt{\sum_m \sum_n \left(spot_{mn} - \overline{spot}\right)^2}\sqrt{\sum_m \sum_n \left([temp_{ij}]_{mn} - \overline{temp_{ij}}\right)^2}} \tag{10}$$

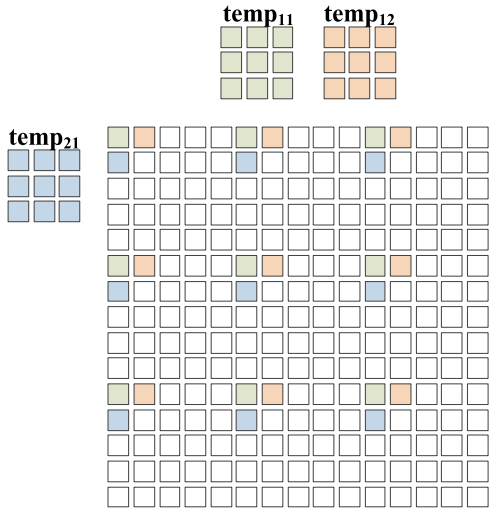

Fig. 3. Schematic of the comparable images' equispaced sampling.

The indices of the maximum PCC in the ρ matrix, represented as *indx* and *indy*, are determined. Finally, the displacement is obtained as follows.

$$\begin{aligned} \Delta x &= (indx - m \times N/2)/N \\ \Delta y &= (indy - n \times N/2)/N \end{aligned} \tag{11}$$

In general, we proposed a method that we believe could perform well in the laser communication system. However, it has a specific requirement for spot size when acting as a general algorithm, and our future research will focus on improving the universality that specific to different spot sizes.

III. Simulation

To evaluate the performance of the proposed method, we simulated the algorithm in several situations and compared results with those of three existing algorithms: CGT, FCG, and GF.

As the simulation must be close to the real application, the simulation parameters such as image size and Gaussian radius

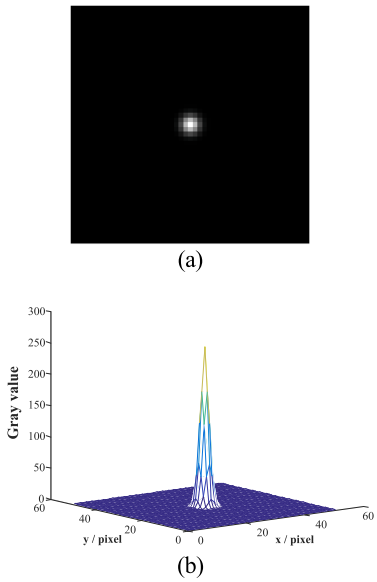

Fig. 4. Ideal laser spot. (a) Gray-scale image. (b) Three-dimensional image.

are determined based on our existing system which could equivalent to most of the similar systems.

In practical applications, the centroid of the laser spot is randomly distributed at various locations, and the location robustness of the algorithm must be evaluated. Therefore, we generated a series of laser spots with different central positions in each situation and compared the mean value and standard deviation of the centroid error, which is defined as follows.

$$error = \sqrt{(x_c - x_0)^2 + (y_c - y_0)^2} \tag{12}$$

where x_c and y_c denote the calculated centroid; and x_0 and y_0 denote the true centroid of the spot.

As for the generation of the images, we consider four parts to form the simulation images: the laser spot, the photon shot noise that related to the intensity of the laser spot, the blind pixels and the Gaussian noise which is equivalent the sum of noises such as Dark noise, readout noise, quantizing noise and thermal noise.

A. Simulation of the Ideal Spot Image

A simulation was performed to verify and compare the theoretical accuracies of the algorithms. The grayscale and 3D images are shown in Fig. 4.

The relevant simulation parameters were set as: the image size was 51 × 51 pixels, and the Gaussian radius was 1.25. The centroid of the laser spot moved from 25.5 to 26.5 along the x- and y-axes. The mean values and standard deviations of the centroid error at different locations are listed in Table I.

In an ideal situation, all the algorithms perform excellently in terms of both absolute error and error stability. Comparatively speaking, the FCG algorithm has the worst performance owing to the change in the gray-scale distribution. The CGT algorithm is better than the FCG algorithm but still has a relatively weak performance, compared with the GF and the proposed method. The mean value and standard deviation of the centroid error

TABLE I
SIMULATION RESULTS OF THE IDEAL SIMULATION

	CGT	FCG	GF	Proposed
Mean value	0.0025	0.0049	0.0016	0.0017
Standard deviation	0.0014	0.0028	0.0013	0.0011

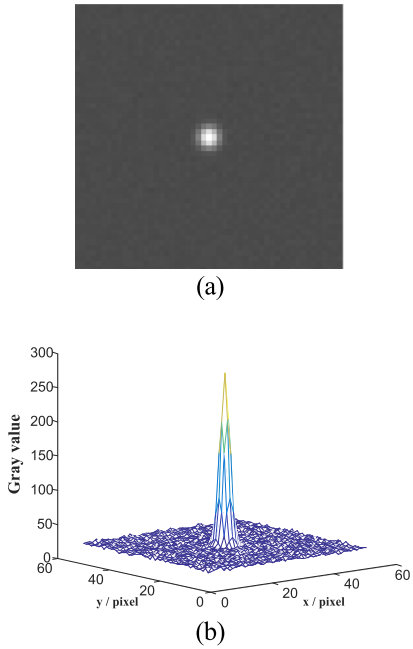

Fig. 5. Laser spot with background noise. (a) Gray-scale image. (b) Three-dimensional image.

calculated using the proposed algorithm were approximately equal to the GF results, indicating that the theoretical accuracy of the proposed algorithm was almost the same as that of the GF algorithm.

B. Simulation of the Spot Image With Background Noise

In an LCT, the photoelectric sensor is typically a short-wave infrared (SWIR) detector, containing background noise owing to non-uniformity. In this section, the performance of the algorithms is verified in the context of background noise, which is equivalent to the imaging results of the SWIR detector. Laser spot images with background noise were generated by adding Gaussian noise. The grayscale and 3D images are presented in Fig. 5.

The simulation was conducted by changing the standard deviation of the noise from 0 to 3, and the relevant simulation parameters for each noise level were set as follows: the image size was 51 × 51 pixels, and the Gaussian radius was 1.25. The centroid of the laser spot moved from 25.5 to 26.5 along the x- and y-axes.

Fig. 6(a) shows the mean values of the centroid error at different locations under different noise levels, and Fig. 6(b)

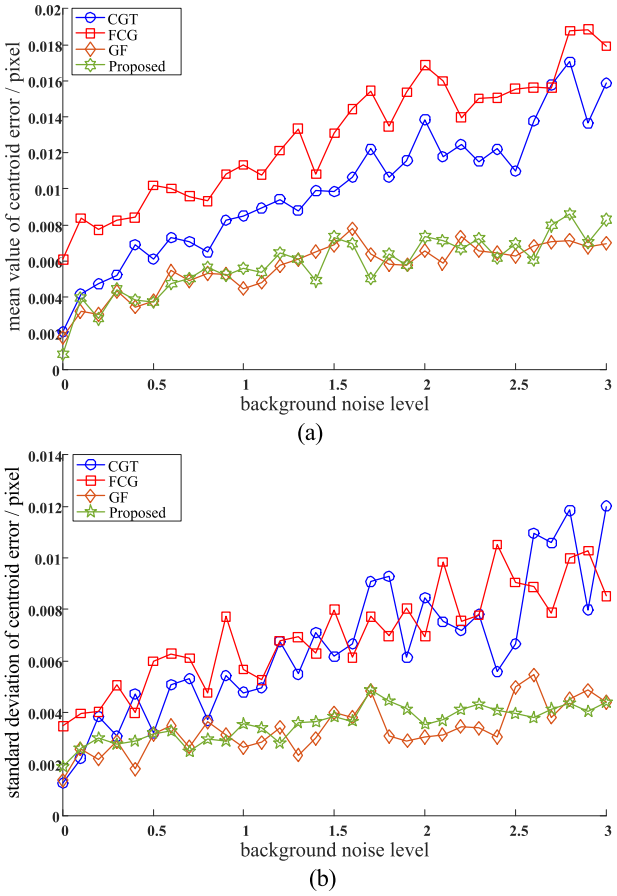

Fig. 6. Centroid error of different locations under different background noise levels. (a) Mean value. (b) Standard deviation.

shows the standard deviations of the centroid error at different locations under different noise levels.

As shown in Fig. 6, the centroid errors of each algorithm increased with noise level. The grey values that constitute the laser spot change with the introduction of noise and affect the calculation results of the CGT and FCG, which use the grey values as weights. This is why the centroid errors of the CGT and FCG rapidly increased compared with those of the GF. The centroid errors of the proposed algorithm are at the same level as those of the GF, thereby indicating that the noise robustness of the proposed method is almost equal to that of the GF and better than that of the other algorithms.

C. Simulation of the Spot Image With Bad Pixels

The simulation in this section focuses on images with bad pixels, which are caused by the degradation of the photosensitive materials of the detector. Laser spot images with bad pixel can be obtained by adding salt and pepper noise. The grayscale and 3D images are shown in Fig. 7.

The simulation was performed under a salt and pepper noise intensity in the range 0–0.03; the standard deviation of the background noise was 3, and the other relevant simulation parameters for each noise intensity are described in Section III-B.

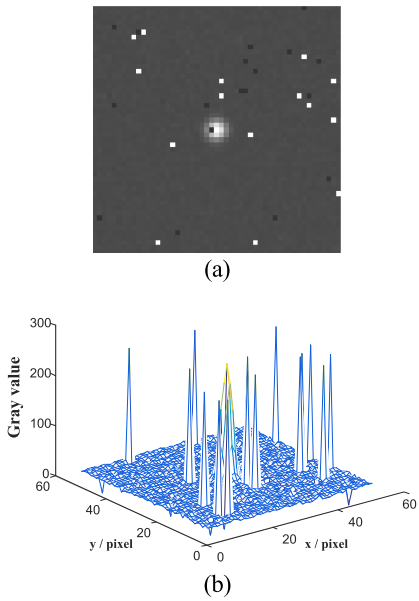

Fig. 7. Laser spot with bad pixels. (a) Gray-scale image. (b) Three-dimensional image.

Fig. 8(a) shows the mean value of the centroid error at different locations under different noise intensities, and Fig. 8(b) shows the standard deviation of the centroid error at different locations under different noise intensities.

The centroid error of the CGT was amplified because of the existence of bad pixels. Because a simple threshold cannot accurately extract the laser spot, pixel values that do not belong to the laser spot are used in the calculation, thereby causing a large error. FCG diminishes the impact of bad pixels with the help of a filter, which is typically a median filter. However, the gray values changed significantly when bad pixels were near or in the laser spot, thereby introducing a relatively larger error. Because the proposed algorithm obtains the centroid by evaluating the correlation that is determined by multiple criteria, such as the absolute value, variation trend, and deviation extent, the robustness to bad pixels is almost the same as that of the GF algorithm, and better than that of other algorithms.

IV. Experimental Verification

A. Experimental Setup

To verify the performance of the proposed algorithm in a hardware system, we established an indoor LCT experimental system, as shown in Fig. 9. The system comprises two components: a collimated laser beam transmitter and a finite aperture receiver.

At the transmitter terminal, a diverging Gaussian beam was emitted from a single-mode fiber endface of the 1565.13 nm laser device, which was mounted on the focal plane of the coarse collimator. The diverging Gaussian beam was shaped by being passed through the coarse collimator followed by being propagated to the fine collimator, which is an off-axis telescope. After propagating through the two collimators, a parallel light equal to the far-field laser distribution was obtained.

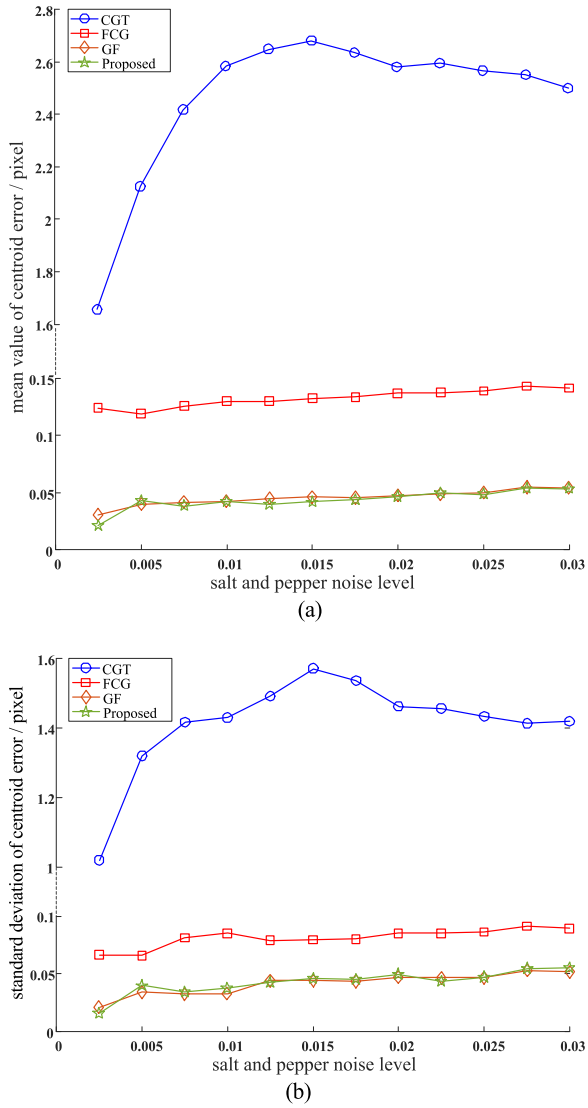

Fig. 8. Centroid error of different locations under different salt and pepper noise intensities with fixed background noise. (a) Mean value. (b) Standard deviation.

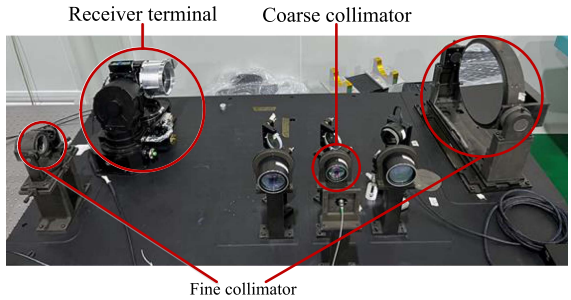

Fig. 9. Laser-communication terminal (LCT) indoor experimental system.

TABLE II
EXPERIMENTAL PARAMETERS

Specifications		Value	Unit
Transmitter	Wavelength	1556.15	nm
	Power	20	dBm
	Focal length	15	m
	Aperture diameter	500	mm
	Simulated Distance	5000	Km
Receiver: optical system	Wavelength	1544.13	nm
	Aperture diameter	100	mm
	Focal length	3	m
Receiver: tracking camera	Frame rates	4000	fps
	Angular resolution	5	μrad
	Total pixels	48×48	pixels
	Laser spot size	5×5	pixels

TABLE III
FRACTIONAL WIDTH ASSIGNMENT

Variables	Fractional width (bits)
Pixel value	0
Mean value Subs value	8
Square value	10
Divisor Dividend	11
Correlation coefficient	22

At the receiver terminal, the finite-aperture telescope converges the incident light and focuses the parallel rays at the focal plane. The SWIR detector then output the laser spot image data to the FPGA, on which the centroid of the laser spot was computed. A telescope was mounted on the gimbal; thus, we could obtain spot images at different locations by controlling the gimbal to move to a certain position.

Table II lists the detailed parameters of the experimental setup.

B. FPGA Implementation

In this section, we describe the FPGA implementation of the proposed algorithm and evaluate its performance. A Xilinx XC4VSX55-10FFG1148I FPGA was used as the processor, and the correlation coefficient shown in (10) was calculated and compared.

The hardware architecture is illustrated in Fig. 10. Considering the timing optimization, compute modules such as the accumulator, multiplier, divider, and multiple accumulators were implemented based on the DSP48 macro block, which improved the calculation efficiency. Some block rams were instantiated as simple dual-port ram or single-port rom to buffer the data used during the calculation to fulfill the timing alignment.

The evaluation of the FPGA implementation focused on the computational accuracy and real-time performance.

The computational accuracy was verified by comparing the results of the FPGA and MATLAB implementations. To optimize the resource usage and computational latency, fixed-point arithmetic was implemented in the FPGA. However, an improper fractional width introduced a truncation error, which affected computational accuracy. Thus, the primary task was to assign

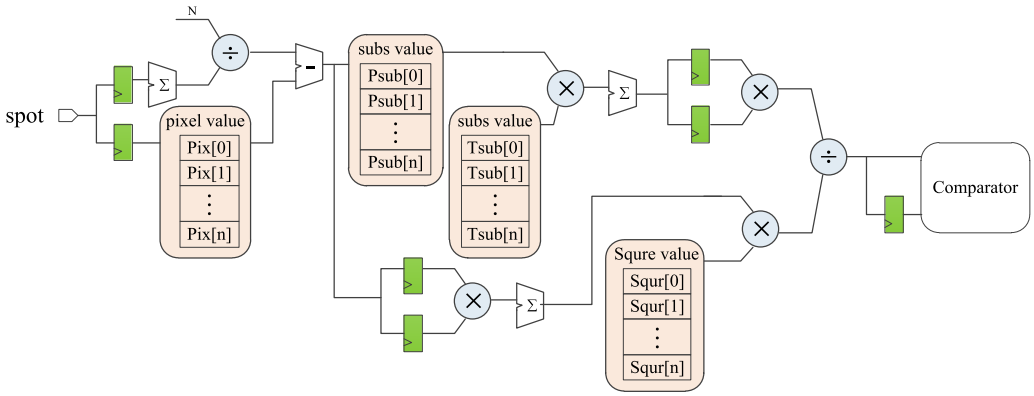

Fig. 10. Hardware architecture of the proposed algorithm.

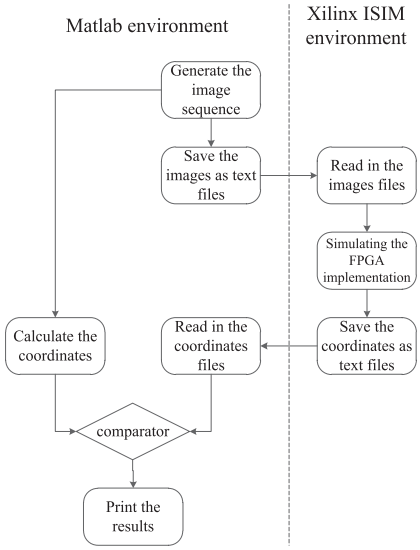

Fig. 11. Flow chart of the computational accuracy verification.

a fractional width during the computation. Table III lists the fractional-width assignments of the variables.

As the aim of the proposed algorithm was to determine the coordinates that correspond to the maximum value, the calculated value differences between the fixed-point (FPGA implementation) and floating-point (MATLAB implementation) are accepted when the maximum value coordinates determined by both arithmetic methods were equal. Computational accuracy verification was conducted using the Xilinx ISIM simulator and MATLAB software. The flowchart is shown in Fig. 11.

The image sequences shown in Fig. 11 were generated based on the three conditions described in Section III, and the comparison results are summarized in Table IV.

The information in Table IV indicates that the FPGA implementation satisfied the computational accuracy requirements.

The following work verifies the real-time performance by using the Xilinx ISIM simulator: As mentioned in Section IV-A, the tracking camera was operated at 4000 fps. The timing sequence of the detector output, which was captured from the camera by an oscilloscope, is shown in Fig. 12.

TABLE IV
COMPARED RESULTS OF THE COMPUTATIONAL ACCURACY VERIFICATION

Verification situation	Image numbers	Same numbers	Different numbers
Ideal spot image	144	144	0
Spot image with background noise	144	144	0
Spot image with bad pixels	144	144	0

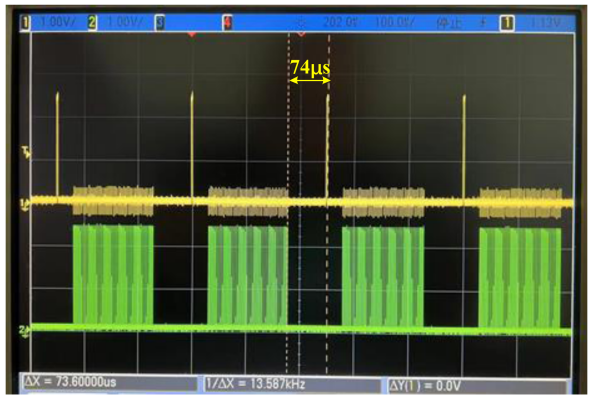

Fig. 12. Timing sequence of the detector output.

The green waveform is the camera-trigger input that controls the image frame to achieve synchronization in the LCT. The yellow waveform represents the horizontal synchronization of the camera, which represents a valid image output period. Fig. 12 shows that the interval between the end of the image and the next frame start is approximately 74 μs. In engineering applications, a master control processor controls a motion actuator at a given time point (within the current frame) in the tracking sequence to achieve stability. The consequent requirement is that the laser spot centroid is calculated before a particular time; thus, the real-time demands for the FPGA implementation are that the centroid of the laser spot should be calculated every 250 μs, and the latency time from the frame start to the centroid output should be less than 245 μs (the control signal calculation and

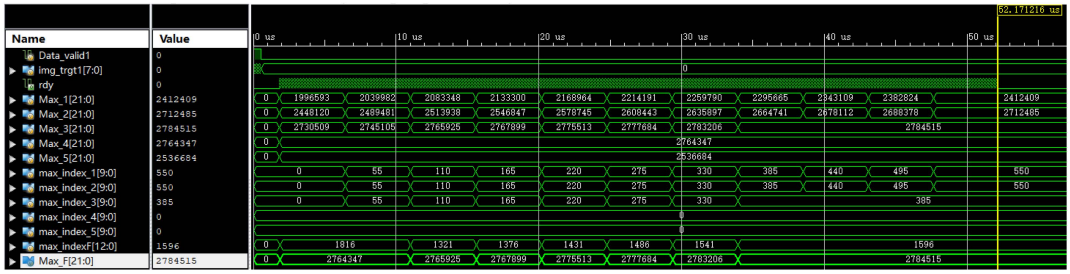

Fig. 13. Real-time simulation of the proposed algorithm.

output take approximately 5 μs). In conclusion, the time required for centroid calculation should be less than 69 μs after the image output is completed.

Based on the above analysis, we conducted a real-time performance verification, in which the laser spot images were generated with background noise ($\sigma = 0.01$). The timing sequence is shown in Fig. 13, and the time consumption of the algorithm is approximately 53 μs, less than the requested 69 μs. Therefore, the real-time performance of the FPGA implementation adheres to engineering requirements.

C. Experiment and Results

The verification experiment was conducted based on the indoor system establishment and FPGA implementation.

The relevant experimental information are summarized as follows. The algorithm is running on the FPGA of tracking camera, which is an important module in LCT. In the indoor system, the LCT acts as the receiver while the transmitter is the synthesis of optical elements. During the experiment, the LCT and the transmitter are all motionless. The experimental parameters are listed in Table II, and the factors that affect the accuracy of the algorithm are brought by the camera itself, there are no external interference.

The procedure of the experiment is as follows. The boresight of the receiver is pointed to the transmitter, and then the gimbal is controlled to rotate to different positions to obtain the laser spot images at different locations of the image plane. For each position, 500–600 images are captured, and the centroid is calculated using CGT, FCG, and the proposed algorithm in real-time, whereas the GF centroid is calculated in MATLAB. Finally, the performances of the four algorithms are evaluated by processing the results in MATLAB.

The experiment was performed at 11 different positions, and the images are shown in Fig. 14.

Because the true value of the laser spot centroid could not be obtained from the captured images, the performance of the algorithm was difficult to evaluate directly. In Ref [19], repeatability, that is, the standard deviation of the centroids at a certain position was used as the evaluation criterion. In Ref [20], the centroid fitted by the GF algorithm was considered as the true value; thus, the centroid error was used to verify the accuracy of the algorithms. In this study, both the repeatability and centroid error were used to evaluate the algorithms. The algorithm with the lowest standard deviation exhibited better repeatability, and

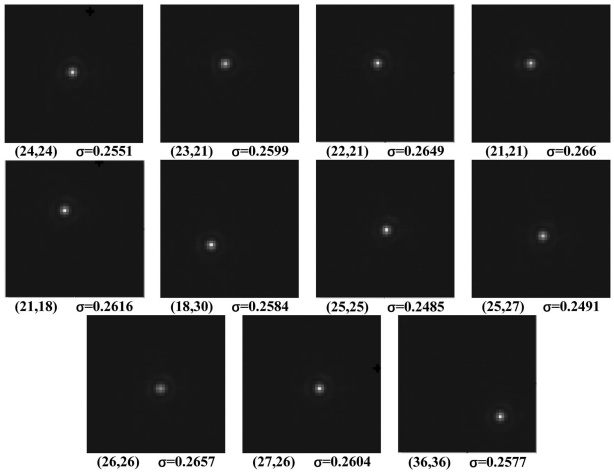

Fig. 14. Images captured by the camera of the system at different positions.

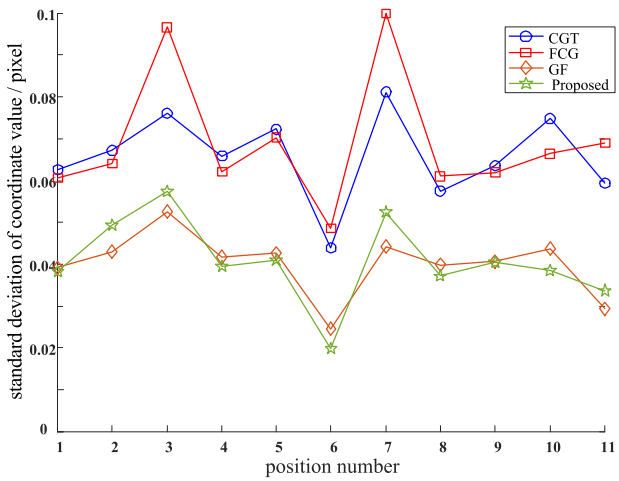

Fig. 15. Standard deviation of the coordinate value at different positions.

the algorithm with the smallest centroid error exhibited better accuracy. The results evaluated using the two criteria are shown in Figs. 15 and 16.

Fig. 15 shows that the standard deviations of the centroids calculated by the proposed algorithm are almost the same as those of the GF, and are smaller at least 30% than those of the CGT and FCG. The results indicate that in terms of repeatability, the proposed algorithm achieves a performance equivalent to that

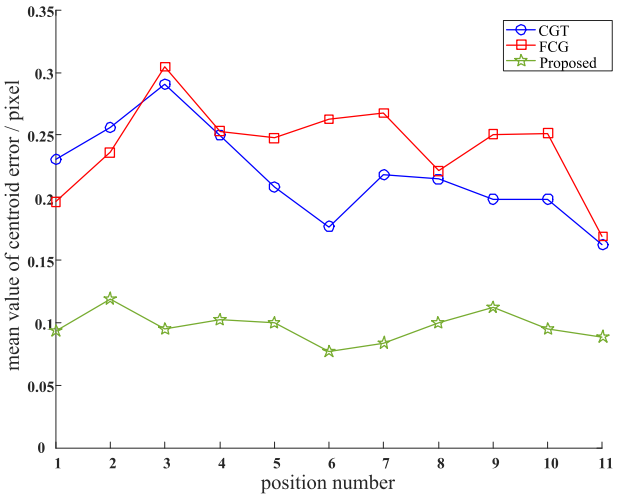

Fig. 16. Mean value of the centroid error at different positions (treat the GF results as true values).

of the GF algorithm, which is better than those of the CGT and FCG algorithms. As for the other criterion, the GF results were used as the true value. We can see in Fig. 16, the centroid errors of the CGT and FCG are in the range 0.2 to 0.3 pixel, which are at least two times bigger than the centroid error calculated by the proposed algorithm. The experimental results indicate that both the stability and the accuracy of the proposed algorithm are perform better than those of the CGT and FCG algorithms, and the proposed algorithm is suitable in terms of accuracy and real-time computations for engineering applications.

V. Conclusion

To overcome the obstacles in accuracy improvement and real-time implementation of existing algorithms, we proposed an algorithm that can achieve a high centroid accuracy that is almost the same as that of the GF algorithm. The proposed algorithm is implemented on an FPGA that ensures that the centroid is output within a single frame time and therefore meets the real-time requirements of engineering applications. Both simulations and experiments verified the performance of the proposed algorithm and confirmed that the proposed algorithm is suitable in terms of accuracy and real-time performance for engineering applications of the inter-satellite laser communications.

References

[1] Z. Xie et al., "Modulator-free variable multi-rate FSO communication 1 km outfield demonstration based on chirp-managed laser," *IEEE Photon. J.*, vol. 14, no. 6, Dec. 2022, Art. no. 7956706, doi: 10.1109/JPHOT.2022.3211268.

[2] H. Kaushal and G. Kaddoum, "Optical communication in space: Challenges and mitigation techniques," *IEEE Commun. Surveys Tuts.*, vol. 19, no. 1, pp. 57–96, Firstquarter 2017, doi: 10.1109/COMST.2016.2603518.

[3] Z. Sodnik, H. Lutz, B. Furch, and R. Meyer, "Optical satellite communications in Europe," *Proc. SPIE*, vol. 7587, Feb. 2010, Art. no. 758705, doi: 10.1117/12.847075.

[4] I. V. Krukova, A. S. Tcherkasov, and N. N. Tchukovsky, "Intersatellite optical communications," in *Proc. Int. Conf. Satell. Commun.*, 1994, pp. 111–112, doi: 10.1109/ICSC.1994.523099.

[5] A. U. Chaudhry and H. Yanikomeroglu, "Laser intersatellite links in a starlink constellation: A classification and analysis," *IEEE Veh. Technol. Mag.*, vol. 16, no. 2, pp. 48–56, Jun. 2021, doi: 10.1109/MVT.2021.3063706.

[6] C. Carrizo, M. Knapek, J. Horwath, D. D. Gonzalez, and P. Cornwell, "Optical inter-satellite link terminals for next generation satellite constellations," *Proc. SPIE*, vol. 11272, pp. 8–18, 2020, doi: 10.1117/12.2545629.

[7] M. Toyoshima, "Recent trends in space laser communications for small satellites and constellations," *J. Lightw. Technol.*, vol. 39, no. 3, pp. 693–699, Feb. 2021, doi: 10.1109/JLT.2020.3009505.

[8] M. Gavrilenko, R. Akbulatov, and R. Lozov, "Free-space laser communication terminal for LEO constellation," in *Proc. Int. Conf. Elect. Eng. Photon.*, 2022, pp. 383–387, doi: 10.1109/EExPolytech56308.2022.9950894.

[9] D. M. Boroson, B. S. Robinson, D. A. Burianek, D. V. Murphy, and A. Biswas, "Overview and status of the lunar laser communications demonstration," *Proc. SPIE*, vol. 8246, Feb. 2012, Art. no. 82460C, doi: 10.1117/12.914801.

[10] W. Wu, M. Chen, Z. Zhang, X. Liu, and Y. Dong, "Overview of deep space laser communication," *Sci. China Inf. Sci.*, vol. 61, no. 4, Apr. 2018, Art. no. 040301, doi: 10.1007/s11432-017-9216-0.

[11] D. M. Boroson, R. S. Bondurant, and J. J. Scozzafava, "Overview of high-rate deep-space laser communications options," *Proc. SPIE*, vol. 5338, pp. 37–49, Jun. 2004, doi: 10.1117/12.543010.

[12] G. D. Wilkins, "The diffraction limited aperture of the atmosphere and its effects on free space laser communications," in *Proc. IEEE Nat. Aerosp. Electron. Conf.@m_NAECON*, 1992, vol. 3, pp. 1158–1163, doi: 10.1109/NAECON.1992.220594.

[13] X. Wan, G. Wang, X. Wei, J. Li, and G. Zhang, "Star centroiding based on fast Gaussian fitting for star sensors," *Sensors*, vol. 18, no. 9, Aug. 2018, Art. no. 2836, doi: 10.3390/s18092836.

[14] B. Zhang, J. Zerubia, and J.-C. Olivo-Marin, "Gaussian approximations of fluorescence microscope point-spread function models," *Appl. Opt.*, vol. 46, no. 10, Apr. 2007, Art. no. 1819, doi: 10.1364/AO.46.001819.

[15] Q. Wang, L. Tong, S. Yu, L. Tan, and J. Ma, "Accurate beacon positioning method for satellite-to-ground optical communication," *Opt. Exp.*, vol. 25, no. 25, Dec. 2017, Art. no. 30996, doi: 10.1364/OE.25.030996.

[16] X. Wei, J. Xu, J. Li, J. Yan, and G. Zhang, "S-curve centroiding error correction for star sensor," *Acta Astronautica*, vol. 99, pp. 231–241, Jun. 2014, doi: 10.1016/j.actaastro.2014.03.002.

[17] X. Ma, C. Rao, and H. Zheng, "Error analysis of CCD-based point source centroid computation under the background light," *Opt. Exp.*, vol. 17, no. 10, May 2009, Art. no. 8525, doi: 10.1364/OE.17.008525.

[18] S. Lee, "Pointing accuracy improvement using model-based noise reduction method," *Proc. SPIE*, vol. 4635, pp. 65–71, Apr. 2002, doi: 10.1117/12.464110.

[19] I. E. Abdou, "Effect of signal truncation on centroid location error estimation," *Opt. Eng.*, vol. 35, no. 4, Apr. 1996, Art. no. 1221, doi: 10.1117/1.600609.

[20] Q. Wang, Y. Liu, Y. Chen, J. Ma, L. Tan, and S. Yu, "Precise locating approach of the beacon based on gray gradient segmentation interpolation in satellite optical communications," *Appl. Opt.*, vol. 56, no. 7, Mar. 2017, Art. no. 1826, doi: 10.1364/AO.56.001826.

[21] L. Tan, Y. Cao, J. Ma, and K. Li, "Optical image centroid prediction based on machine learning for laser satellite communication," *Opt. Exp.*, vol. 27, no. 19, Sep. 2019, Art. no. 26615, doi: 10.1364/OE.27.026615.

[22] S. Yang, X. Ke, D. Sun, J. Liang, and Y. Zhang, "Kalman filter spot centroid detection algorithm in optical wireless communication," *Opt. Eng.*, vol. 61, no. 5, May 2022, Art. no. 056104, doi: 10.1117/1.OE.61.5.056104.

[23] X. Meng, C. Ma, Y. Tian, J. Han, and D. Liang, "Research on high precision locating of laser spot center in free-space laser communication system," in *Proc. IEEE 5th Inf. Technol., Netw., Electron. Automat. Control Conf.*, 2021, pp. 1625–1629, doi: 10.1109/ITNEC52019.2021.9587297.

[24] S. Chen, "Realization and optimization of fine tracking system of free space laser communication," *J. Infrared Millimeter Waves*, vol. 37, no. 1, pp. 35–41, Feb. 2018, doi: 10.11972/j.issn.1001-9014.2018.01.008.

[25] L. Sheugh and S. H. Alizadeh, "A note on Pearson correlation coefficient as a metric of similarity in recommender system," in *Proc. AI Robot.*, 2015, pp. 1–6, doi: 10.1109/RIOS.2015.7270736.